GKSS
FORSCHUNGSZENTRUM
in der HELMHOLTZ-GEMEINSCHAFT

Preprint 2010

Efficient computation of the elastography inverse problem by combining variational mesh adaption and a clustering technique

A. Arnold, S. Reichling,
O. T. Bruhns and J. Mosler

This is a preprint of an article accepted by:

Physics in Medicine and Biology (2010)

GKSS Research Centre Geesthacht
Materials Mechanics

Efficient computation of the elastography inverse problem by combining variational mesh adaption and a clustering technique

A. Arnold, S. Reichling and O.T. Bruhns

Institute of Mechanics
Ruhr University Bochum
Ruhr University Bochum
D-44780 Bochum, Germany
E-Mail: bruhns@tm.bi.rub.de

J. Mosler

Materials Mechanics
Institute for Materials Research
GKSS Research Centre
D-21502 Geesthacht, Germany
E-Mail: joern.mosler@gkss.de

SUMMARY

This paper is concerned with an efficient implementation suitable for the elastography inverse problem. More precisely, the novel algorithm allows to compute the unknown stiffness distribution in soft tissue by means of the measured displacement field by reducing the numerical cost considerably compared to previous approaches. This is realized by combining and further elaborating variational mesh adaption with a clustering technique similar to those known from, digital image compression. Within the variational mesh adaption, the underlying finite element discretization is only locally refined, if this leads to a considerable improvement of the numerical solution. Additionally, the numerical complexity is reduced by the aforementioned clustering technique, in which the parameters describing the stiffness of the respective soft tissue are sorted according to a pre-defined number of intervals. By doing so, the number of unknowns associated with the elastography inverse problem can be chosen explicitly. A positive side effect of this method is the reduction of artificial noise in the data (smoothing of the solution). The performance and the rate of convergence of the resulting numerical formulation are critically analyzed by numerical examples.

1 Introduction

Elasticity imaging or elastography is a powerful method for visualizing the stiffness distribution in soft tissue in vivo, cf. [1–7]. Conceptually, the deformation is measured first by comparing ultrasound or MRI signals of a tissue sample before and after prescribing a certain loading and subsequently, by applying correlation-based algorithms or by minimization of a suitable objective function, see [8, 9]. The computed deformation field serves as input data for an inverse analysis allowing to determine the underlying stiffness distribution. Since pathologies affect in many cases the stiffness, elastography is very promising for detecting such critical regions. More precisely, diseased tissue tends to be stiffer than the surrounding material. This is particularly common in breast cancer and prostate tumors where hard lumps are usually observed.

The aforementioned inverse problem can either be solved by employing direct methods or by using iterative algorithms. For a comprehensive overview and a critical review of such approaches, the reader is referred to [3–5, 10, 11]. From a computational point of

view, direct methods are more efficient. However, they can only be applied to relatively simple boundary value problems, i.e., fully linearized models. Furthermore, the extensions necessary for anisotropic materials are cumbersome. By way of contrast, iterative schemes do not show such constraints. Fully nonlinear mechanical problems and different mechanical responses can easily be included. This is particular important for modeling biological tissue showing a pronounced anisotropic and nonlinear mechanical behavior. Conceptually, iterative approaches are based on a minimization problem. More precisely, a certain distance between the measured and the computed deformation field is minimized depending on the unknown stiffness distribution. Though this idea is relatively simple, its numerical implementation is, unfortunately, not straightforward. The reasons for that are manifold. First, the function to be minimized is highly nonlinear. Second, several minima exist and the measured displacement data show a certain noise. However, from a numerical point of view, the probably most serious problem is the singularity of the minimization problem (the Hessian is singular). Fortunately, by applying regularization techniques, the aforementioned problems can be eliminated (except for the first of those being not crucial), i.e., the modified minimization problem is locally well-posed. Implementations suitable for solving this modified optimization problem can be found in [3–5, 12, 13].

As mentioned before, elasticity imaging or elastography is a very promising technique for detecting hard lumps characteristic of breast cancer and prostate tumors. Clearly, a successful application of such a method in practice relies crucially on its efficiency. Though the measuring of the displacement field by ultrasound or MRI signals, together with certain filtering techniques, is numerically very efficient, the computation of the resulting inverse problem is far from being real-time. For that reason, two novel techniques are discussed and elaborated in the paper. Each of them increases the efficiency significantly.

The implementation of the inverse problem is based on a finite element discretization. Since only rate-independent material behavior is considered in the presented paper, the spatial triangulation is the only factor governing the accuracy of the algorithm. However, it defines the numerical efficiency as well. More precisely, a refined mesh leads to a better resolution of the stiffness distribution, while increasing the associated numerical cost. Hence, it is reasonable to refine the mesh only, if this results in a considerable improvement of the numerical solution. Concerning elastography, regions showing a high gradient of the material stiffness or interfaces between different materials are to be refined. Obviously, such regions are not known a priori. Following [14, 15], adaptive finite element discretization can be applied for detecting them. Roughly, an error estimate is computed first and subsequently, the triangulation is refined accordingly. Though such approaches are mathematically very elegant, they can only be applied, if several constraints are fulfilled. For instance, error estimation requires linearity of the underlying Hilbert space, cf. [16]. Clearly, this condition is not met here. For this reason and following [17], so-called variational mesh adaptions are employed and further elaborated. Such methods depend crucially on the underlying minimization problem and are meaningful regardless of the linear or nonlinear structure of the problem and do not presuppose a linear-much less normed-structure of the space of solutions (cf, e. g., [18]). Conceptually, if $I(\mu)$ denotes the functional to be minimized (depending on the unknown distribution of the material parameter μ), an approximate solution μ_2 is better than another approximation solution μ_1, if and only if $I(\mu_2) < I(\mu_1)$. Since the canonically induced error indicator $\Delta I = I(\mu_1) - I(\mu_2)$ requires thus the computation of two optimization problems, it is numerically very expensive. For that reason, it is estimated. The resulting algorithm shows linear $\mathcal{O}(n)$ complexity.

By applying the aforementioned novel variational mesh adaption, the efficiency of the algorithm suitable for solving the inverse problem associated with elastography can be increased significantly. However, the ultimate goal being a real-time analysis is still out of range. Hence, the algorithm is combined with another method further accelerating the numerical formulation. More precisely, the advocated variational mesh adaption is coupled to a clustering technique similar to those applied in digital image compression. Analogously to [19, 20], the material parameters are sorted according to a predefined number of groups. By doing so, the number of degrees of freedom can be controlled and consequently, the efficiency is directly affected. Illustrative examples show that this filtering technique does not lead to a loss in accuracy. By contrast, it reduces artificial noise (smoothing of the solution).

The paper is organized as follows: Section 2 is concerned with the forward problem, i.e., with the standard boundary value problem of continuum mechanics. Having briefly introduced the adopted material model, focus is on a locking-free numerical implementation by means of a mixed finite element formulation. The associated inverse problem is addressed in Section 3. Though the presented framework shows several differences compared to previous publications such as the material model, the mixed finite element formulation or the definition of the objective function, the core contribution of the paper is discussed in Sections 4 and 5. While the novel variational mesh adaption is presented in Section 4, Section 5 is concerned with the aforementioned clustering technique.

2 The forward problem of hyperelasticity

This section is concerned with a concise review of the classical forward problem of nonlinear continuum mechanics. Consequently and in line with other boundary value problems in physics, the boundary conditions such as prescribed stresses or displacements, together with the material parameters, are assumed to be given. Based on these input data, the forward problem of nonlinear continuum mechanics is the computation of the unknown deformation of the considered body. Since in the present paper, the modeling of biological tissue represents the area of application, focus is on hyperelastic material models, i.e., conservative systems. While the fundamentals associated with the aforementioned forward problem are briefly discussed in Subsection 2.1, the corresponding numerical implementation by means of the finite element method is addressed in Subsection 2.2. Further details on nonlinear continuum mechanics and hyperelastic materials can be found in the comprehensive overviews [21–23].

2.1 Fundamentals

In what follows, the conservative mechanical system associated with hyperelasticity is considered. The hyperelastic solid occupying a domain $\mathcal{B}_0$ in its reference undeformed configuration is assumed to undergo quasistatic deformations under the action of prescribed externally applied loads and displacement boundaries, see figure 1. The deformation is usually described by introducing the nonlinear function $\boldsymbol{\varphi}(\mathbf{X})$ mapping the position of a material point in the reference configuration $\mathbf{X} \in \mathcal{B}_0$ to its deformed position $\mathbf{x} \in \mathcal{B}_t$. Evidently, relative deformations or displacements $\mathbf{u}$ are measured in experiments. They are related to $\boldsymbol{\varphi}$ by $\mathbf{u}(\mathbf{X}) = \boldsymbol{\varphi}(\mathbf{X}) - \mathbf{X}$. Locally, the deformation mapping $\boldsymbol{\varphi}$ is approximated by the deformation gradient $\mathbf{F} = \mathrm{GRAD}\boldsymbol{\varphi} := \partial\mathbf{x}/\partial\mathbf{X}$. Based on $\mathbf{F}$ strain measures such as the right Cauchy-Green tensor $\mathbf{C} = \mathbf{F}^T \cdot \mathbf{F}$ can be derived.

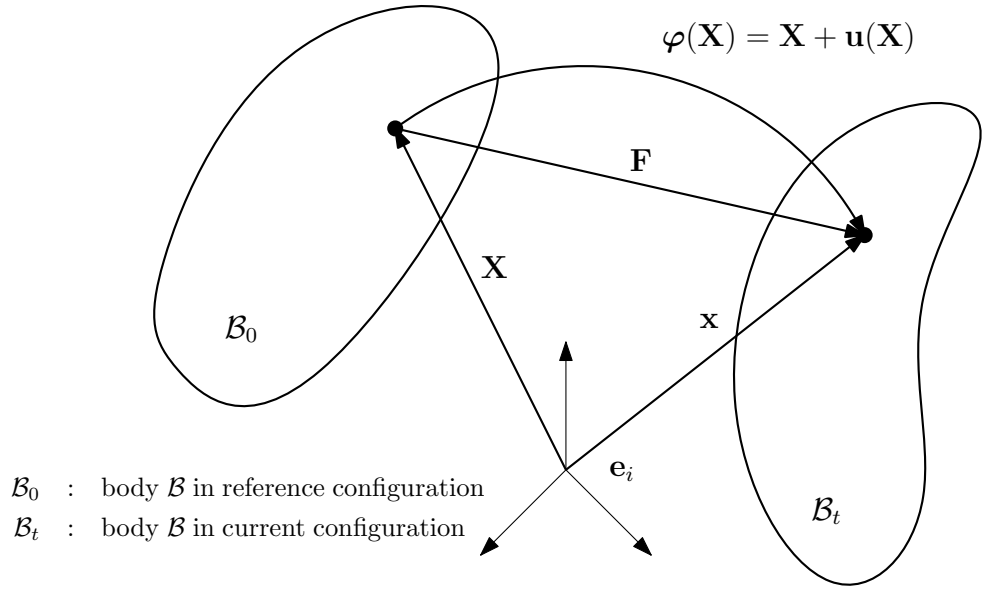

Figure 1: Reference and current configuration: Deformation of the body $\mathcal{B}$

Since only hyperelastic material models are considered in the present paper, the reversible stored energy W is the function defining uniquely every aspect of the mechanical response. Clearly, W is subjected to some constraints such as the requirement of objectivity $W = W(\mathbf{F}) = \hat{W}(\mathbf{C})$ and certain growth conditions. By inserting $W = W(\mathbf{F})$ into the dissipation inequality and by enforcing reversibility, the stress tensor predicted by the hyperelastic model can be derived. More precisely, the first Piola-Kirchhoff stress tensor yields

$$\mathbf{P} = \frac{\partial W(\mathbf{F})}{\partial \mathbf{F}}. \tag{1}$$

In what follows, a certain Neo-Hooke-type constitutive model is adopted. It is based on an isochoric-volumetric split of the energy function, i.e.,

$$W(\hat{\mathbf{C}}, J) = W(\hat{\mathbf{C}}) + U(J). \tag{2}$$

Here, $J := \det \mathbf{F}$ is the Jacobian determinant measuring the change in volume ($J = \mathrm{d}v/\mathrm{d}V$) and $\hat{\mathbf{C}}$ represents an isochoric right Cauchy-Green strain tensor, i.e.,

$$\hat{\mathbf{C}} := \hat{\mathbf{F}}^T \cdot \hat{\mathbf{F}}, \quad \text{with} \quad \hat{\mathbf{F}} := J^{-1/3}\, \mathbf{F} \quad \Rightarrow \quad \det \hat{\mathbf{F}} = 1. \tag{3}$$

Models based on the decomposition (2) are frequently applied in solid mechanics, particularly to biological tissues, cf. [24]. In the present paper, the volumetric and the deviatoric part of the energy are defined by means of two material parameters: the shear modulus μ and the bulk modulus K. More precisely, the following energies are adopted:

$$W(\hat{\mathbf{C}}) := \frac{1}{2}\mu \left(I_{\hat{C}} - 3\right), \quad U(J) := \frac{K}{4}\left(J^2 - 1\right) - \frac{K}{2} \ln J \tag{4}$$

where $I_{\hat{C}} := \mathrm{tr}(\hat{\mathbf{C}})$ is the first invariant of the isochoric right Cauchy-Green tensor $\hat{\mathbf{C}}$, cf. [25]. By applying (1), the first Piola-Kirchhoff stress tensor results in the additive decomposition

$$\mathbf{P} = \mathbf{P}_{\mathrm{iso}} + \mathbf{P}_{\mathrm{vol}} \tag{5}$$

with

$$\mathbf{P}_{\text{iso}} = \frac{\partial W(\hat{\mathbf{C}})}{\partial \mathbf{F}} = \mu J^{-\frac{2}{3}} \left(\mathbf{F} - \frac{1}{3} \operatorname{tr}(\mathbf{C})\, \mathbf{F}^{-T} \right) \tag{6}$$

$$\mathbf{P}_{\text{vol}} = \frac{\partial U}{\partial \mathbf{F}} = pJ\mathbf{F}^{-T}, \quad p := \frac{\partial U}{\partial J}. \tag{7}$$

Here and henceforth, p is the hydrostatic pressure.

It is well known that for hyperelastic solids, the unknown deformation mapping $\boldsymbol{\varphi}$ follows naturally from minimizing the potential energy of the mechanical system, if the body is subjected to quasi-static conservative loadings. The local or strong form of the respective stationarity conditions reads

$$\operatorname{Div} \mathbf{P} = \rho\, \mathbf{b} \tag{8}$$

$$\mathbf{u} = \bar{\mathbf{u}} \qquad \forall \mathbf{X} \in \partial\mathcal{B}_{0u} \tag{9}$$

$$\mathbf{P} \cdot \mathbf{N} = \bar{\mathbf{t}} \qquad \forall \mathbf{X} \in \partial\mathcal{B}_{0\sigma}. \tag{10}$$

Here, $\mathbf{N}$, ρ, $\mathbf{b}$ and Div denote the outward unit normal vector at $\partial\mathcal{B}_0$, the (referential) density, prescribed body forces and the (referential) divergence operator, respectively. $\partial\mathcal{B}_0 = \partial\mathcal{B}_{0u} \cup \partial\mathcal{B}_{0\sigma}$ represents the boundary of $\mathcal{B}_0$, which can be disjunctively split into one part $\partial\mathcal{B}_{0\sigma}$ where the tractions are defined and one part $\partial\mathcal{B}_{0u}$ associated with the prescribed displacements $\bar{\mathbf{u}}$.

Since the response function $\mathbf{P} = \mathbf{P}(\mathbf{F})$ is highly nonlinear, the resulting boundary value problem (8)–(10) can only be analytically solved for relatively simple problems. Usually, numerical strategies such as the finite element method are required. For applying this method, the weak form associated with (8)–(10) is required. Clearly, the weak form can be derived in standard manner, i.e., by multiplying the strong form by a suitable test function and subsequently, applying an integration. However, since the considered mechanical problem is conservative, the principle of minimum potential energy is utilized, cf. [26]. The potential energy $\Pi = \Pi_{\text{int}} + \Pi_{\text{ext}}$ to be minimized can be subdivided additively into an internal part Π_{int} being the integrated strain energy density and an external part Π_{ext} due to prescribed forces, i.e.,

$$\Pi_{\text{int}} = \int_{\mathcal{B}_0} W(\mathbf{F})\, \mathrm{d}V \tag{11}$$

$$\Pi_{\text{ext}} = -\int_{\mathcal{B}_0} \boldsymbol{\varphi} \cdot \rho\bar{\mathbf{b}}\, \mathrm{d}V - \int_{\partial\mathcal{B}_{0\sigma}} \boldsymbol{\varphi} \cdot \bar{\mathbf{t}}\, \mathrm{d}A, \qquad \bar{\mathbf{t}} := \mathbf{P} \cdot \mathbf{N}|_{\partial\mathcal{B}_{0\sigma}}. \tag{12}$$

It can be shown in a simple manner that a minimization of Π with respect to the unknown deformation mapping $\boldsymbol{\varphi}$ is equivalent to the strong form (8)–(10). However, since biological tissue is almost incompressible, a straightforward discretization of $\inf \Pi(\boldsymbol{\varphi})$ by using finite elements would lead to pathological numerical locking effects, cf. [27]. Hence, an enhanced variational method is adopted. Following [28, 29], a Hu-Washizu principle in terms of the primary variables deformation $\boldsymbol{\varphi}$, pressure p and volumetric strain Θ is employed. Without going too much into details, the resulting variational problem reads (cf. [23])

$$\operatorname{stat}\Pi^{\text{HW}}(\boldsymbol{\varphi}, p, \Theta) = \operatorname{stat} \left\{ \int_{\mathcal{B}_0} W(\hat{\mathbf{C}}) + U(\Theta) + p(J - \Theta)\, \mathrm{d}V + \Pi_{\text{ext}}(\boldsymbol{\varphi}) \right\} \tag{13}$$

and its corresponding stationarity conditions are given by

$$\mathrm{D}_\Theta \Pi^{\mathrm{HW}} \, \gamma = \int_{\mathcal{B}_0} \gamma \left(\frac{\partial U(\Theta)}{\partial \Theta} - p \right) \, \mathrm{d}V = 0 \tag{14}$$

$$\mathrm{D}_p \Pi^{\mathrm{HW}} \, q = \int_{\mathcal{B}_0} q \, (J - \Theta) \, \mathrm{d}V = 0 \,, \tag{15}$$

$$\mathrm{D}_{\boldsymbol{\varphi}} \Pi^{\mathrm{HW}} \cdot \boldsymbol{\eta} = \int_{\mathcal{B}_0} \mathrm{Grad}\, \boldsymbol{\eta} : (\mathbf{P}_{\mathrm{iso}} + \mathbf{P}_{\mathrm{vol}}) \, \mathrm{d}V = 0 \tag{16}$$

where γ, q and $\boldsymbol{\eta}$ are the variations of the volumetric strain Θ, the variations of the pressure p and the variations of the displacement field $\mathbf{u}$, respectively. Furthermore, $\mathrm{D}_a \Pi^{\mathrm{HW}}$ denotes the partial derivative of Π^{HW} with respect to a. For the sake of simplicity, prescribed forces have been neglected in (16) and an energy functional W of the type (2)-(4) yielding the additive decomposition (5) of the stress tensor $\mathbf{P} = \mathbf{P}_{\mathrm{iso}} + \mathbf{P}_{\mathrm{vol}}$ has been assumed. The applied numerical implementation is based on a finite element discretization of the weak forms (14)-(16). Such a technique is nowadays standard. Further details can be found, for instance, in [27, 30]. Nevertheless, for the sake of understandability, the algorithmic formulation is briefly discussed in the following subsection.

2.2 Numerical implementation

The finite element discretization of (14)-(16) is based on an approximation of the primary variables $\mathbf{x} = \boldsymbol{\varphi}$, θ and p and their corresponding variations $\boldsymbol{\eta}$, γ and q. As usually, the approximation of a variable $(\bullet)$ is denoted by a the index h, i.e., $(\bullet)^h$ and the notation $(\bullet)_e$ is used to highlight that the approximation is defined elementwise. With these definitions, the following Bubnov-Galerkin-type discretizations are employed:

$$\mathbf{x}_e^h = \sum_{I=1}^{n_1} N_I^{\varphi}(\boldsymbol{\xi}) \mathbf{x}^I \in \mathbb{P}_2 \cap \mathcal{C} \qquad \boldsymbol{\eta}_e^h = \textstyle\sum_{I=1}^{n_1} N_I^{\varphi}(\boldsymbol{\xi}) \boldsymbol{\eta}^I \in \mathbb{P}_2 \cap \mathcal{C} \tag{17}$$

$$\theta_e^h = \sum_{I=1}^{n_2} N_I^{\theta}(\boldsymbol{\xi}) \theta^I \in \mathbb{P}_0 \qquad \gamma_e^h = \textstyle\sum_{I=1}^{n_2} N_I^{\theta}(\boldsymbol{\xi}) \gamma^I \in \mathbb{P}_0 \tag{18}$$

$$p^h = \sum_{I=1}^{n_3} N_I^{p}(\boldsymbol{\xi}) p^I \in \mathbb{P}_0 \qquad q_e^h = \textstyle\sum_{I=1}^{n_3} N_I^{p}(\boldsymbol{\xi}) q^I \in \mathbb{P}_0. \tag{19}$$

Here, $\mathbb{P}_i$ is the space containing all polynomials of order i, $\mathcal{C}$ is the space of continuous functions, N_I^a denotes the shape function corresponding to node I and $\mathbf{x}^I$ are the respective nodal deformations. The geometry of the undeformed configuration is approximated by adopting an isoparametric concept, i.e.,

$$\mathbf{X}_e^h = \sum_{I=1}^{n_1} N_I^{\varphi}(\boldsymbol{\xi}) \mathbf{X}^I \in \mathbb{P}_2 \cap \mathcal{C}. \tag{20}$$

Inserting (17) into the weak form (16), the contribution of element e to the stationarity condition (16) with respect to the nodal variable $\boldsymbol{\eta}^I$ reads

$$\boldsymbol{\eta}^I \cdot \mathbf{r}_e^I = 0 \quad \text{with} \quad \mathbf{r}_e^I := \int_{\mathcal{B}_0^e} (\mathbf{P}_{\mathrm{iso}} + \mathbf{P}_{\mathrm{vol}}) \cdot \frac{\partial N_I^{\varphi}}{\partial \mathbf{X}_e^h} \, \mathrm{d}V_e \,. \tag{21}$$

Clearly, a classical assembling procedure has to be applied to such element contributions resulting in the global stationarity condition associated with the considered mechanical system.

The resulting set of nonlinear equations is solved by applying Newton's scheme. Consequently, the linearization of (21) is required. With $\mathbf{P}_{\text{iso}} = \mathbf{P}_{\text{iso}}(\mathbf{F})$ and $\mathbf{P}_{\text{vol}} = \mathbf{P}_{\text{vol}}(\mathbf{F}, p)$, it is obtained as

$$\begin{aligned}\Delta(\mathrm{D}_{\varphi}\Pi^{\text{HW}} \cdot \boldsymbol{\eta}) &= \int_{\mathcal{B}_0} \operatorname{Grad}\boldsymbol{\eta} : \Delta(\mathbf{P}_{\text{iso}} + \mathbf{P}_{\text{vol}})\,\mathrm{d}V \\ &= \int_{\mathcal{B}_0} \operatorname{Grad}\boldsymbol{\eta} : \left(\frac{\partial(\mathbf{P}_{\text{iso}} + \mathbf{P}_{\text{vol}})}{\partial \mathbf{F}} : \Delta\mathbf{F} + J\mathbf{F}^{-T}\Delta p\right)\,\mathrm{d}V.\end{aligned} \tag{22}$$

The rate in pressure Δp can be computed by linearizing (14) and (15), i.e. from equations

$$\Delta(\mathrm{D}_{\Theta}\Pi^{\text{HW}}\ \gamma) = \int_{\mathcal{B}_0} \gamma\left(\frac{\partial^2 U(\Theta)}{\partial\Theta^2}\Delta\Theta - \Delta p\right)\,\mathrm{d}V = 0 \tag{23}$$

$$\Delta(\mathrm{D}_{p}\Pi^{\text{HW}}\ q) = \int_{\mathcal{B}_0} q\left(J\,\mathbf{F}^{-T} : \Delta\mathbf{F} - \Delta\Theta\right)\,\mathrm{d}V = 0\,. \tag{24}$$

More precisely, (23) and (24) allow to compute Δp as a function in terms of $\Delta\mathbf{F}$. Since the deformation gradient depends only on the unknown deformation, i.e., $\mathbf{F}_e^h = \mathbf{F}_e^h(\mathbf{x}^I)$, (21) represents eventually a nonlinear set of equations depending exclusively on the unknown nodal deformations $\mathbf{x}^I$. The respective linearization of $\mathbf{r}_e^I$ is thus given by

$$\boldsymbol{\eta}^I \cdot \Delta\mathbf{r}_e^I = \boldsymbol{\eta}_I \cdot \mathbf{k}_e^{IJ} \cdot \Delta\mathbf{x}^J \qquad \text{with} \quad \mathbf{k}_e^{IJ} = \hat{\mathbf{k}}_e^{IJ} + \bar{\mathbf{k}}_e^{IJ}. \tag{25}$$

The stiffness matrices $\hat{\mathbf{k}}_e^{IJ}$ and $\bar{\mathbf{k}}_e^{IJ}$ are computed as

$$\hat{\mathbf{k}}_e^{IJ} = \int_{\mathcal{B}_0^e} \frac{\partial N^I}{\partial \mathbf{X}} \overset{(2)}{\cdot} \frac{\partial(\mathbf{P}_{\text{iso}} + \mathbf{P}_{\text{vol}})}{\partial \mathbf{F}} \cdot \frac{\partial N^J}{\partial \mathbf{X}}\,\mathrm{d}V_e \tag{26}$$

$$\bar{\mathbf{k}}_e^{IJ} = \int_{\mathcal{B}_0^e} J\mathbf{F}^{-T} \cdot \frac{\partial N^I}{\partial \mathbf{X}} \otimes \bar{\mathbf{m}}^J\,\mathrm{d}V_e. \tag{27}$$

In (26), $\overset{(2)}{\cdot}$ indicates that the simple contraction has to be applied to the second index, e.g., $(\partial N^I/\partial\mathbf{X} \overset{(2)}{\cdot} \partial\mathbf{P}/\partial\mathbf{F})_{ijk} = (\partial N^I/\partial\mathbf{X})_l\ (\partial\mathbf{P}\partial/\mathbf{F})_{iljk}$. The matrix $\bar{\mathbf{m}}^J$ in (27) is the sensitivity of the pressure with respect to the deformation at node J, i.e., $\Delta p_e^h = \sum_{J=1}^{n_1} \bar{\mathbf{m}}^J \cdot \Delta\mathbf{x}^J$ with

$$\bar{\mathbf{m}}^J = \frac{1}{V_e}\int_{\mathcal{B}_0^e} \frac{\partial^2 U(\Theta)}{\partial\Theta^2}\,\mathrm{d}V_e \frac{1}{V_e}\int_{\mathcal{B}_0^e} J\mathbf{F}^{-T} \cdot \frac{\partial N^J}{\partial\mathbf{X}}\,\mathrm{d}V_e. \tag{28}$$

It is obtained from the set of equations (23) and (24).

The assembling of the element stiffness matrices yields finally the global stiffness matrix denoted as $[\mathbf{k}]$. With $[\mathbf{r}]$ and $[\mathbf{x}]$ being the global vector of internal forces and the collection of all nodal deformations, Newton's scheme requires to solve the linear problem $[\mathbf{k}][\Delta\mathbf{x}] = [\mathbf{r}]$. For that purpose, the powerful solver PARDISO 3.2 is utilized, cf. [31, 32].

3 The inverse problem of hyperelasticity

In contrast to the forward problem of hyperelasticity discussed in the previous section, the corresponding inverse problem is addressed here. Hence, the deformation mapping, together with the Neumann boundary conditions, is assumed to be known, while the distribution of the material parameters is to be computed. More precisely, since almost incompressible biological tissue represents the area of application in the present paper, the bulk modulus can be considered as very high and constant. Consequently, the distribution of the shear modulus is the only unknown. In Subsection 3.1, the fundamentals of this inverse problem, including the respective numerical implementation, are briefly presented. A numerical example demonstrating the applicability as well as the performance of the resulting algorithmic formulations is presented in Subsection 3.2.

3.1 Fundamentals

Evidently, the inverse problem of hyperelasticity which is frequently referred to as the *inverse problem of elasticity imaging* can be stated as a classical minimization problem. For that purpose and in line with [5, 7, 12], the functional

$$\mathfrak{g}(\mu) = \frac{1}{2}\|\mathcal{P}(\boldsymbol{\varphi} - \boldsymbol{\varphi}^g)\|^2 + \frac{\alpha}{2}\|\mu - \mu^*\|^2 \rightarrow \min \tag{29}$$

depending on the unknown shear modulus distribution μ is introduced. In (29), $\boldsymbol{\varphi} = \boldsymbol{\varphi}(\mu)$, $\boldsymbol{\varphi}^g$, $\mathcal{P}$, α and μ^* denote the deformation mapping in terms of the unknown shear modulus, the measured or given deformation, a projection operator defined as $\mathcal{P}(\boldsymbol{\varphi}) = \varphi_2$, a regularization parameter and a reference shear modulus distribution. The projection $\mathcal{P}$ reflects that only the axial component (X_2-direction) of the deformation can be measured (sufficiently accurately). As expected, the unrelaxed problem (29) minimizes the error between measured and computed deformation mapping. However, this problem is usually highly ill-conditioned and several minima exist. Therefore, the second term in (29) being a Tikhonov-type regularization is required, cf. [33]. Physically, this term means that only a relative shear modulus distribution can usually be determined. More precisely, if $\mu^{(1)}$ is a minimizer, $\mu^{(2)} = a\,\mu^{(1)}\ \forall a \in \mathbb{R}$ defines a family of equivalent minimizers. By adding the relaxation term, one of these solutions is selected.

The minimization problem

$$\inf_{\mu} \mathfrak{g}(\mu) \tag{30}$$

is solved by utilizing the L-BFGS-B algorithm, see [34, 35]. This method belongs to the class of quasi Newton schemes and approximates the Hessian of $\mathfrak{g}$ by means of the gradient of $\mathfrak{g}$. Therefore, the functional $\mathfrak{g}(\mu)$ and the gradient $\mathrm{D}_\mu\mathfrak{g}$ have to be computed within each iteration step. In line with the forward problem, this is done by applying the finite element method. Consequently, the functional $\mathfrak{g}(\mu)$ is approximated by

$$\mathfrak{g}(\mu) \approx \mathfrak{g}^h(\mu^h) = \sum_{e=1}^{n} \mathfrak{g}_e^h(\mu_e^h)\,, \tag{31}$$

where n is the number of elements within the discretization. According to (29), the contribution of each element e is given by

$$\mathfrak{g}_e^h(\mu_e^h) = \frac{1}{2}\int_{\mathcal{B}_{0e}} ({x_2}_e^h - x_{2e}^{gh})^2\,\mathrm{d}V_e + \frac{\alpha}{2}\int_{\mathcal{B}_{0e}} (\mu_e^h - {\mu^*}_e^h)^2\,\mathrm{d}V_e. \tag{32}$$

Here, ${x_2}_e^h$ are the computed nodal deformations depending on the shear modulus distribution and ${x_2}_e^{gh}$ represent the measured counterparts. Furthermore, μ_e^h denotes the current and ${\mu^*}_e^h$ the reference shear modulus. The gradient $\mathrm{D}_{\mu^h}\mathfrak{g}$ necessary for the aforementioned L-BFGS-B algorithm can be computed by linearizing $\mathfrak{g}$. Denoting the linearization of a field a^h with respect to the shear modulus as $\Delta^{\mu^h} a^h$, the contribution of an element e to this gradient reads

$$\begin{aligned}\Delta^{\mu^h}\mathfrak{g}_e^h &= \mathrm{D}_{\mu^h}\mathfrak{g}_e^h \cdot \Delta\mu_e^h \\ &= \int_{\mathcal{B}_{0^e}} ({x_2}_e^h - {x_2}_e^{gh})(\Delta^{\mu^h}{x_2}_e^h)\, dV_e + \alpha \int_{\mathcal{B}_{0^e}} (\mu_e^h - {\mu^*}_e^h)\Delta\mu_e^h\, dV_e.\end{aligned} \tag{33}$$

According to (33), the linearization of the deformation with respect to the shear modulus distribution is required, i.e., $\Delta^{\mu^h}{x_2}_e^h = \Delta^{\mu^h}{x_2}_e^h(\Delta\mu_e^h)$. This sensitivity can be computed by linearizing the weak form of equilibrium (16) yielding

$$\mathrm{D}_\mu(\mathrm{D}_\varphi \Pi^{\mathrm{HW}} \cdot \boldsymbol{\eta}) \cdot \Delta\mu = \int_{\mathcal{B}_0} \mathrm{Grad}\,\boldsymbol{\eta} : [\mathrm{D}_\mu \mathbf{P}(\boldsymbol{\varphi}, p, \Theta) \cdot \Delta\mu]\ \mathrm{d}V = 0. \tag{34}$$

Inserting

$$\begin{aligned}&\mathrm{D}_\mu \mathbf{P}(\boldsymbol{\varphi}, p, \Theta) \cdot \Delta\mu = \\ &\quad \mathrm{D}_\mu \mathbf{P} \cdot \Delta\boldsymbol{\mu} + \mathrm{D}_\varphi \mathbf{P} \cdot \Delta^\mu \boldsymbol{\varphi} + \mathrm{D}_p \mathbf{P} \cdot \Delta^\mu p + \mathrm{D}_\Theta \mathbf{P} \cdot \Delta^\mu \Theta\end{aligned} \tag{35}$$

into (34), together with the linearizations

$$\mathrm{D}_\mu \mathbf{P} \cdot \Delta\boldsymbol{\mu} = J^{-\frac{2}{3}} \left(\mathbf{F} - \frac{1}{3} \mathrm{tr}\,(\mathbf{C})\, \mathbf{F}^{-T} \right)\ \Delta\mu \tag{36}$$

$$\mathrm{D}_\varphi \mathbf{P} \cdot \Delta^\mu \boldsymbol{\varphi} = \frac{\partial \mathbf{P}}{\partial \mathbf{F}} : \mathrm{Grad}\,(\Delta^\mu \boldsymbol{\varphi}) \tag{37}$$

$$\mathrm{D}_p \mathbf{P} \cdot \Delta^\mu p = J\mathbf{F}^{-T} \Delta^\mu p \tag{38}$$

$$\mathrm{D}_\Theta \mathbf{P} \cdot \Delta^\mu \Theta = 0 \tag{39}$$

results finally in

$$\boldsymbol{\eta}^I \cdot \mathbf{k}_e^{IJ} \cdot \Delta^{\mu^h}\mathbf{x}^J = \boldsymbol{\eta}_I \cdot \mathbf{p}_e^I\ \Delta\mu \qquad \text{with} \quad \mathbf{p}_e^I = \hat{\mathbf{p}}_e^I + \bar{\mathbf{p}}_e^I. \tag{40}$$

The matrices $\hat{\mathbf{p}}_e^I$ and $\bar{\mathbf{p}}_e^I$ are computed as

$$\hat{\mathbf{p}}_e^I := \int_{\mathcal{B}_0^e} \left[J^{-\frac{2}{3}} \left(\mathbf{F} - \frac{1}{3} \mathrm{tr}\,(\mathbf{C})\, \mathbf{F}^{-T} \right) \right] \cdot \frac{\partial N^I}{\partial \mathbf{X}}\ \mathrm{d}V_e \tag{41}$$

$$\bar{\mathbf{p}}_e^I := \int_{\mathcal{B}_0^e} \left[\left(J\mathbf{F}^{-T} \right) m_{\bar{p}_e} \right] \cdot \frac{\partial N^I}{\partial \mathbf{X}}\ \mathrm{d}V_e. \tag{42}$$

where $m_{\bar{p}_e}$ is the sensitivity of the pressure with respect to the shear modulus, i.e.,

$$m_{\bar{p}_e} := \frac{1}{V_e} \int_{\mathcal{B}_0^e} \frac{1}{\mu} \frac{\partial U(\Theta)}{\partial \Theta} \mathrm{d}V_e. \tag{43}$$

The assembling of the element stiffness matrices and application of the adjoint method yields finally the gradient $\mathrm{D}_\mu \mathfrak{g}$. Further details about the adjoint method can be found in [5, 12].

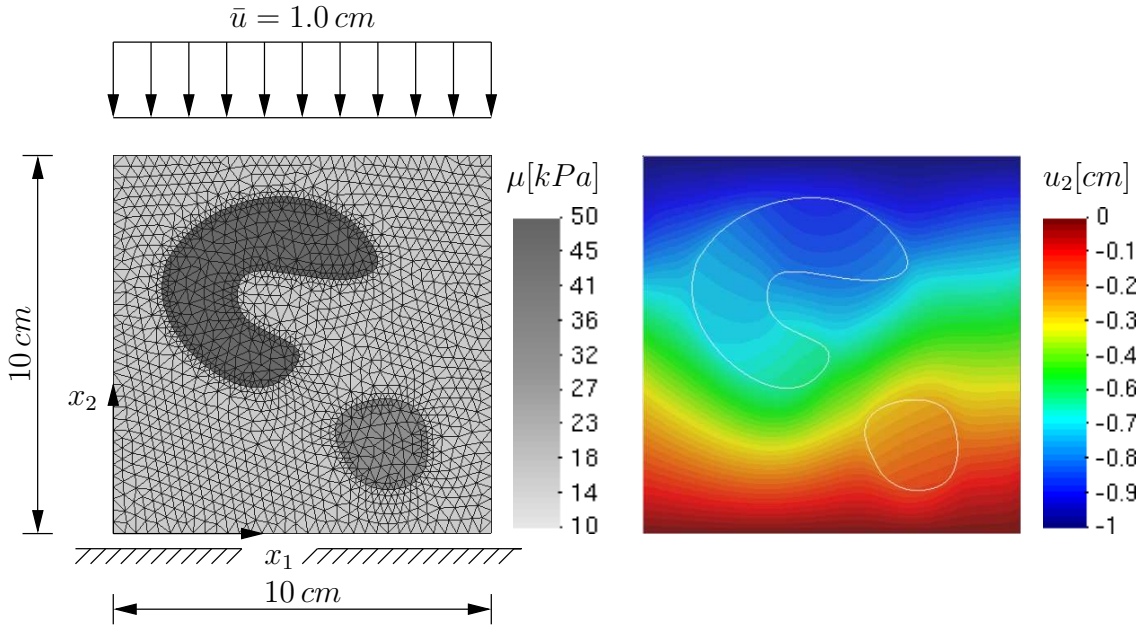

Figure 2: Compression test of biological tissue with two hard lumps: a) geometry, stiffness distribution of the shear modulus and boundary conditions, b) computed displacement field

Remark 3.1 *According to (32), the error between the measured and the computationally predicted displacement field is defined by means of the L_2-norm. Clearly, other norms are admissible as well. More precisely, if a finite element discretization is considered leading to a finite dimensional approximation, all norms are mathematically equivalent. In the numerical examples, a slightly different norm has thus been adopted. More precisely, the norm $||f||_{\text{norm}} := 1/V \int_V f\,dV$ independent of the size of the respective finite element has been employed. By doing so, the influence of small elements (those at the interfaces) becomes more important.*

3.2 Numerical example

The applicability as well as the performance of the proposed numerical formulation are demonstrated in this subsection. For that purpose, a classical forward problem is considered first, see figure 2. Subsequently, the computed displacement field is utilized as input data for an inverse analysis. According to figure 2, the mechanical problem is a compression test of biological tissue showing two hard lumps. The ratio of the shear moduli is assumed to be $\mu_{inc1}/\mu_{inc2}/\mu_{mat} = 5/3/1$. Here, μ_{mat}, μ_{inc1} and μ_{inc2} are the material parameters associated with the bulk, the larger inclusion and that corresponding to the smaller lump. In the whole domain a Poisson's ratio of $\nu = 0.48$ is adopted. The employed mixed finite element formulation is based on a quadratic interpolation of the geometry and the deformation, while the pressure, the volumetric strain and the shear modulus distribution are approximated as piecewise constant, cf. (17)–(19). As evident from figure 2, it is almost impossible to estimate the number and the topologies of the hard lumps based on the displacement field.

Next, the inverse problem is considered. The displacement field shown in figure 2 serves as input data, while the shear modulus distribution is now the unknown variable. The inverse problem is solved by using the algorithm described in Section 3, combined

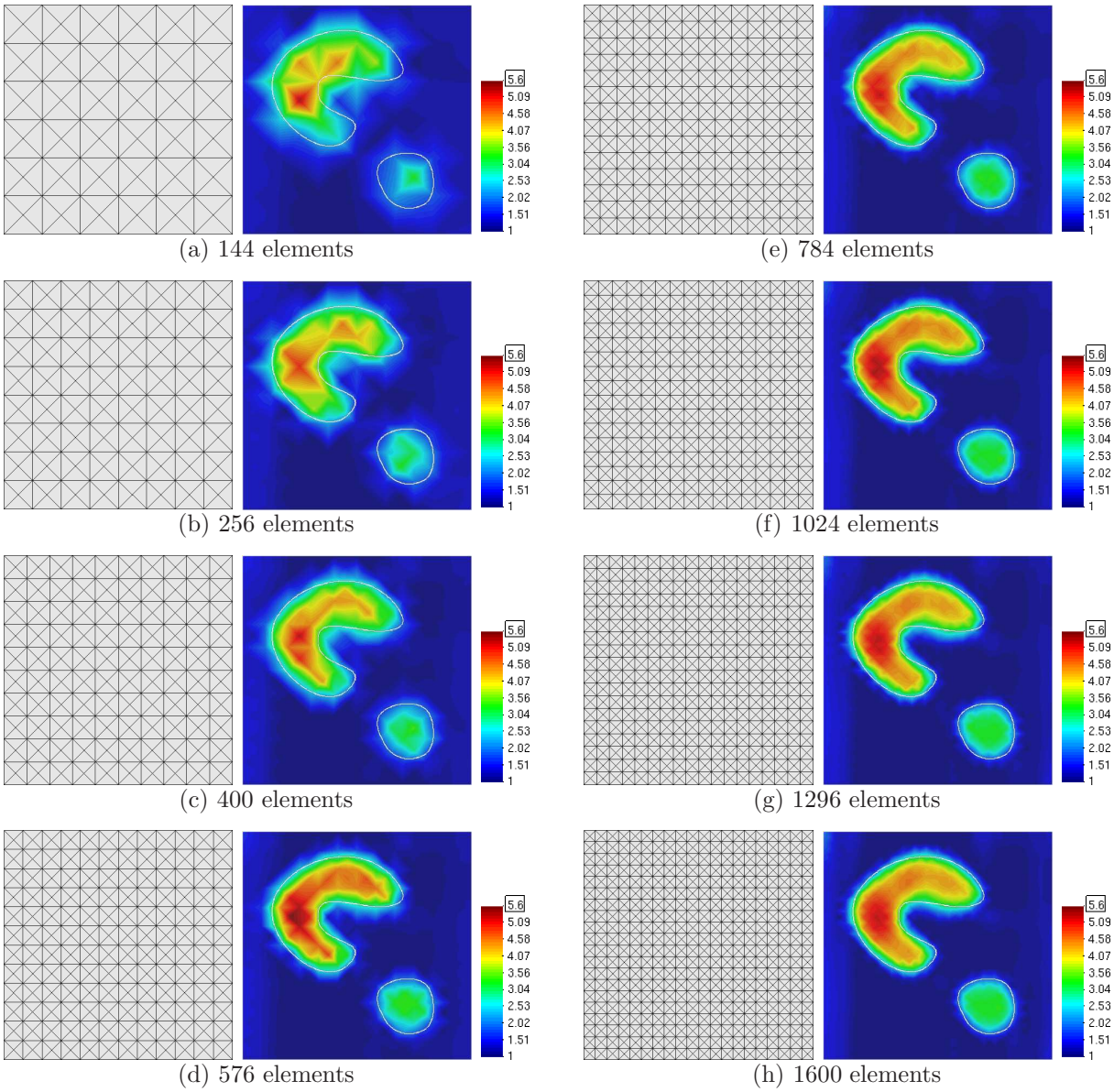

(a) 144 elements (e) 784 elements

(b) 256 elements (f) 1024 elements

(c) 400 elements (g) 1296 elements

(d) 576 elements (h) 1600 elements

Figure 3: Compression test of biological tissue with two hard lumps: Computed shear modulus distribution for different uniform mesh refinement steps

with an L-BFGS-B scheme. The initial value of the shear modulus is set to $\mu = 1$. Since the displacement field is noise free, the regularization term can be neglected, i.e., $\alpha = 0$, see (29). Figure 3 shows the results obtained from the inverse analysis by using different finite element discretizations. Each discretization is uniform and almost isotropic. More precisely, all elements are geometrically equivalent and within each triangulation, the diameter of the elements is constant as well. According to figure 3, the coarse mesh leads to a relatively poor approximation of the shear modulus distribution. With an increasing number of elements, the quality of the numerical solution improves significantly and interfaces between different materials are better localized. Clearly, this is a direct consequence of the space of shear modulus approximations. The finer the discretization, the larger is that space.

The accuracy of the predicted shear modulus distribution depending on the considered finite element discretization is shown in figure 4. According to that figure, the difference between the measured (forward problem) and the computed displacement field

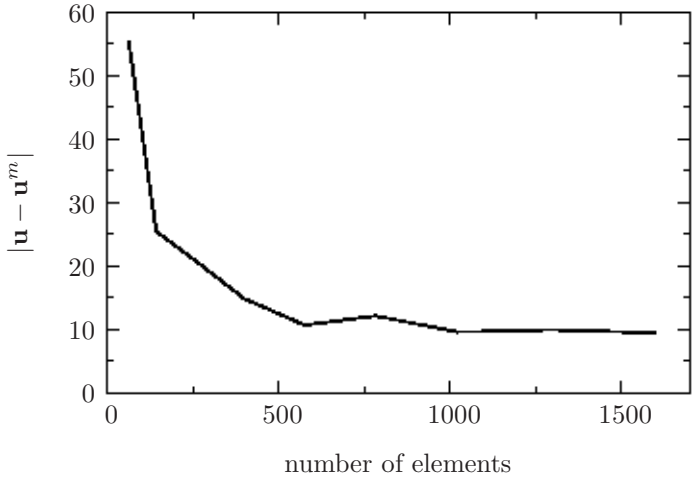

Figure 4: Compression test of biological tissue with two hard lumps: Difference between computed and measured displacement field depending on the number of elements (uniform mesh refinement)

(inverse problem) decreases with an increasing number of elements. However, the respective curve does not decrease monotonically. The reason for this is twofold. First, the numerical computations depend slightly on the termination criterion used in the L-BFGS-B algorithm. The reported results were obtained by employing the criteria $(\mathfrak{g}(\mu^i) - \mathfrak{g}(\mu^{i-5}))/(\mathfrak{g}(\mu^{i-5})) < 0,01$ and $\mathfrak{g}(\mu^i) < 1,0 \cdot 10^{-18}$. Second, and even more importantly, a monotone convergence can only be expected if the approximation spaces of shear moduli are nested. However, according to figure 3, this is not always the case. Clearly, mesh (d) can be generated by subdividing the elements of mesh (a) and therefore, the resulting approximation space is indeed a superset. Thus, the respective shear modulus approximation is guaranteed to be better than that of mesh (a). This is in agreement with figure 3. However, some of the discretizations are evidently not nested and hence, such a relation does not hold anymore.

In summary, the applicability of the proposed algorithm for solving the inverse problem was clearly demonstrated by the analyzed example. Furthermore, the solution quality depends indeed on the underlying finite element discretization. As usual, the higher the numerical cost (fine discretization, large number of degrees of freedom), the better is the approximation. Since the numerical complexity of the proposed algorithmic formulation is relatively high, an adaptive scheme, combined with a clustering technique, is presented in what follows. The resulting method shows a high accuracy by reducing the numerical cost significantly.

4 Variational h-refinement

The algorithmic formulation discussed in the previous section is based on the finite element method. Consequently, the quality of the numerical solution depends on the approximation of the field variables such as the displacements. The approximation, in turn, is defined by the interpolations within the considered finite element (see (17)–(20)) and the triangulation. In this section, an h-adaptive scheme is presented. Hence, the shape functions are not modified and the quality of the approximation is improved be refining the discretization in regions of interest, e.g., at interfaces between different materials.

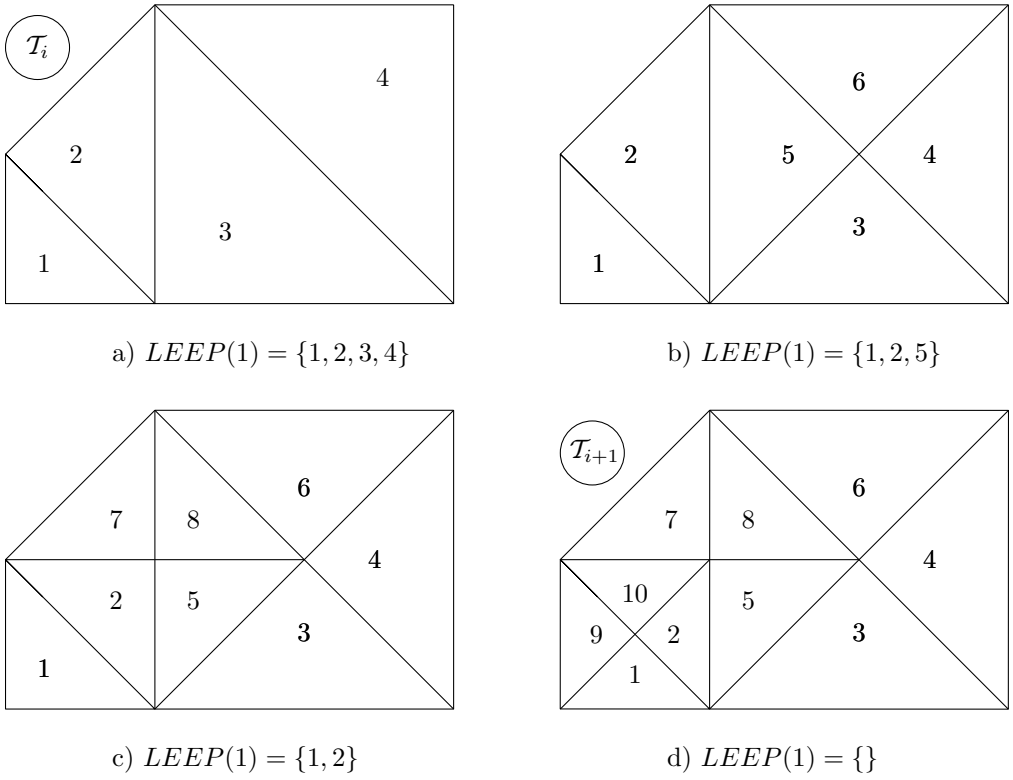

a) $LEEP(1) = \{1, 2, 3, 4\}$ b) $LEEP(1) = \{1, 2, 5\}$

c) $LEEP(1) = \{1, 2\}$ d) $LEEP(1) = \{\}$

Figure 5: LEPP-algorithm according to Rivara, cf. [36, 37]: Element 1 is refined by subdividing the elements according to the LEPP. *Definition of LEPP:* The LEPP of a triangle is the ordered list of all triangles such that t_i is the neighbor triangle of t_{i-1} by the longest side.

4.1 Fundamentals

Conceptually, the finite element triangulation replaces the original problem

$$\inf_{\mu} \mathfrak{g}(\mu) \quad \mu \in V^{\mu}, \quad \text{with} \quad \dim V^{\mu} = \infty \tag{44}$$

by the finite-dimensional counterpart

$$\inf_{\mu} \mathfrak{g}(\mu) \quad \mu \in V^{h_\mu}, \quad \text{with} \quad \dim V_0^{h_\mu} = n < \infty. \tag{45}$$

Clearly, the quality of the numerical solution is increased by enlarging the space of admissible shear modulus distributions $V_0^{h_\mu}$. More precisely,

$$\inf_{\mu \in V_1^{h_\mu}} \mathfrak{g}(\mu) \leq \inf_{\mu \in V_0^{h_\mu}} \mathfrak{g}(\mu), \quad \text{if} \quad V_1^{h_\mu} \supset V_0^{h_\mu}. \tag{46}$$

In the following, nested series of triangulations of the type $V_n^{h_\mu} \supset \ldots \supset V_1^{h_\mu} \supset V_0^{h_\mu}$ will be considered. Hence, regardless of the nonlinear structure of the inverse problem, the numerical approximation is indeed improved. The series of meshes is generated by edge-bisection. More specifically, Rivara's algorithm based on the Longest-Edge-Propagation-Path (LEPP) is utilized, cf. [36, 37]. An illustration of this method is depicted in figure 5. In what follows, $\mathcal{T}_{i+1,e=j}$ denotes the triangulation obtained by applying Rivara's LEPP-algorithm to element j of the initial discretization $\mathcal{T}_i$.

Though a refinement of the underlying finite element mesh leads to an improvement of the numerical approximation, it results in a larger number of degrees of freedom and therefore, in higher numerical cost. For that reason, it is important to refine only those elements which are located in critical regions. In other words, elements are to be subdivided, only if this leads to a significant improvement of the solution. The selection of such elements relies usually on error estimates or error indicators. For an overview, the interested reader is referred to [14, 15] and references cited therein. Clearly, from a mathematical point of view, error estimates, are stronger and hence, they are preferable. However, such estimates require the existence, uniqueness and a certain regularity of the solution, together with linearity of the problem, cf. [16]. Unfortunately, those requirements are not met here. As a consequence, a so-called *variational* error indicator will be utilized, cf. [17, 38–43]. It is noteworthy that this error indicator is equivalent to a rigorous mathematical error estimate in case of linear problems, see [17, 44] and Remark 4.1.

According to the variational structure of (45), the overriding criterion that governs every aspect of the system is (energy) minimization. Therefore, it is natural to allow the same principle to drive mesh adaption as well. Such methods are referred to as *variational mesh adaption*, cf. [38, 41–43]. In the context of the classical forward problem, they date back, at least to [45] (see also [46] and references therein). In the cited papers, the nodal positions of a discretization are optimized by using the underlying variational structure. These methods are known as *variational r-adaptions*. In the present paper, a different method is proposed. In line with [17, 44], a natural error indicator induced by the variational framework is derived. Though mathematically speaking, it is only an error estimate for certain cases, it guarantees that the solution is improved. In this respect, it can be considered as in between an estimate and an indicator, cf. Remark 4.1.

Following [43], every minimum principle implies a natural distance which can be used for comparing the quality of different approximations. More precisely, consider the two solution μ_0^h and μ_1^h. Then, $\mu_1^h \in V_1^{h_\mu}$ is better than $\mu_0^h \in V_0^{h_\mu}$, if and only if $\inf_{\mu\in V_1^{h_\mu}} \mathfrak{g}(\mu) \leq \inf_{\mu\in V_0^{h_\mu}} \mathfrak{g}(\mu)$. Based on this observation, an error indicator of the type

$$\Delta\mathfrak{g}_j^{\mathrm{ref}} = \inf \mathfrak{g}(\mathcal{T}_i) - \inf \mathfrak{g}(\mathcal{T}_{i+1,e=j}), \quad \mathcal{T}_i \subset \mathcal{T}_{i+1,e=j} \tag{47}$$

can be introduced. Again, $\mathcal{T}_{i+1,e=j}$ denotes the triangulation obtained by applying Rivara's LEPP-algorithm to element j of the initial discretization $\mathcal{T}_i$. According to (47), $\Delta\mathfrak{g}_j^{\mathrm{ref}}$ measures the effect of a local mesh refinement of element j on the solution.

Although the aforementioned error indicator is mathematically and physically sound, it is numerically very expensive, i.e., a global optimization problem has to be solved for every possible local refinement step. Therefore, and in line with [43], the conservative estimate $\Delta\bar{\mathfrak{g}}_j^{\mathrm{ref}}$ defined as

$$\begin{aligned} 0 \leq \Delta\bar{\mathfrak{g}}_j^{\mathrm{ref}} := \quad & \inf_{\mu_i^h \in V_i^{h_\mu}} \mathfrak{g}(\mathcal{T}_i) \\ & - \inf_{\substack{\mu_{i+1}^h \in V_{i+1,e=j}^{h_\mu} \\ \mathrm{supp}(\mu_{i+1}^h - \mu_i^h) = \mathrm{supp}(V_{i+1,e=j}^{h_\mu}/V_i^{h_\mu})}} \mathfrak{g}(\mathcal{T}_{i+1,e=j}) \leq \Delta\mathfrak{g}_j^{\mathrm{ref}} \end{aligned} \tag{48}$$

is introduced. In contrast to the global estimate (47), (48) is based on a local approximation, i.e., the functional $\mathfrak{g}(\mathcal{T}_{i+1,e=j})$ is minimized by relaxing the old solution $\inf \mathfrak{g}(\mathcal{T}_i)$ only in a certain neighborhood. According to (48), this local neighborhood is chosen as that spanned by the refined elements. Since the size of the aforementioned neighborhood is

independent of the size of the global discretization, the resulting algorithm shows a linear complexity $\mathcal{O}(n)$ and thus, it is very efficient.

The quality of estimate (48) can be improved by relaxing the old solution within a larger neighborhood. However, as demonstrated in [17, 44], choosing $\mathrm{supp}(\mu_{i+1}^h - \mu_i^h)$ as local neighborhood leads to reasonable results. Further details on the presented variational indicator are omitted. For the classical forward problem, a detailed discussion may be found in [17, 44].

Remark 4.1 *According to [17, 44], the variational error indicator (48) is formally identical to so-called* hierarchical basis error estimates *(cf. [14]), i.e., the error is estimated by comparing the finite element solution to that corresponding to a higher order approximation. In the present paper, this higher-order space is designed by h-refinement (edge bisection). In case of fully linear problems (the function to be minimized is quadratic), it can be further shown, that the variational error indicator (48) is equivalent to the aforementioned hierarchical error estimate. As a consequence, in this case, it shows the same properties such as efficiency or optimality, cf. [14]. However, it bears emphasis that the objective function considered within the present paper is highly nonlinear. Consequently, the error indicator (48) is not an error estimate (strictly mathematically speaking) and thus, definitions such as optimality do not apply any more.*

Remark 4.2 *For the sake of comparison, an additional error indicator is defined as well. Though it is related to the mathematical error induced by the finite element approximation, it is purely heuristic. More precisely, the functional* $\mathfrak{g}$ *itself represents the error to be minimized. Hence, it is reasonable to analyze the respective element contributions. This argumentation leads to the indicator*

$$\Delta\bar{\mathfrak{g}}_j^{ref} = \mathfrak{g}_{e=j}(\mu_{e=j}^h). \tag{49}$$

In what follows, it is denoted as indicator II.

4.2 Numerical example

The performance and the accuracy of the variational adaptive finite element method compared to those of a uniform mesh refinement are analyzed in this subsection. The computation starts with the same initial discretization as shown in figure 3(a). Subsequently, the algorithm discussed in the previous subsection is applied. The so obtained triangulation is used as new input for the next refinement step. In each of such steps, the elements are ordered according to their variational error indicator. 20% of the elements showing the largest values are eventually refined by applying Rivara's LEPP algorithm. Clearly, other criteria can be applied as well.

For some representative refinement steps, the computed shear modulus distribution and the respective discretization are collected in figure 6. Starting with a relatively poor approximation, the quality of the solution improves fast by refining the triangulation according to the variational error indicator. Already after 4 steps, the distribution of the shear modulus is captured reasonably well by requiring only 287 finite elements. The final discretization consisting of 2116 elements shows a very fine mesh at the interfaces between different materials, while a relatively coarse mesh is observed in the remaining part of the domain. Thus, only critical regions are refined. Clearly, this leads to a high efficiency of the resulting algorithmic formulation.

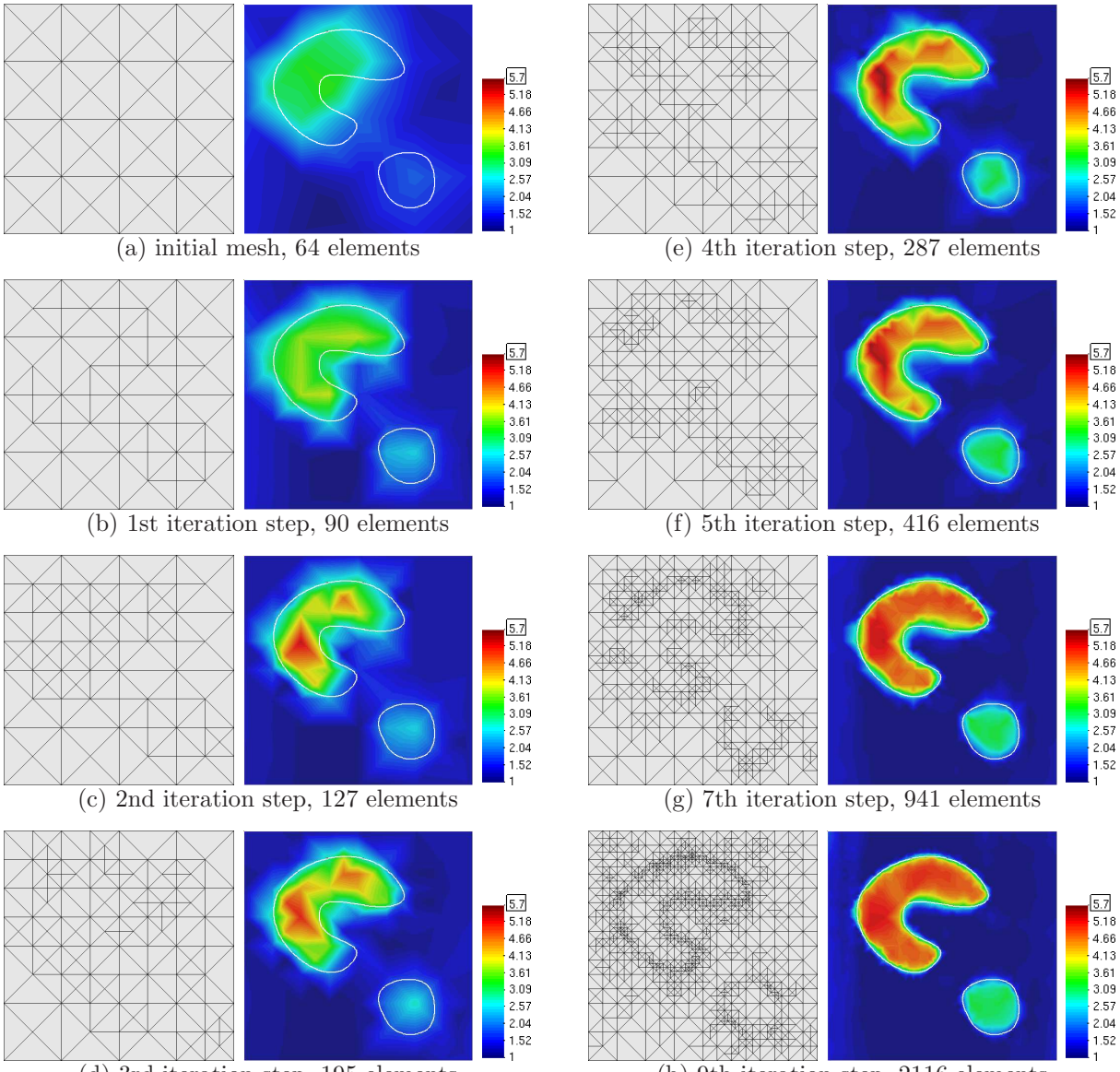

(a) initial mesh, 64 elements

(b) 1st iteration step, 90 elements

(c) 2nd iteration step, 127 elements

(d) 3rd iteration step, 195 elements

(e) 4th iteration step, 287 elements

(f) 5th iteration step, 416 elements

(g) 7th iteration step, 941 elements

(h) 9th iteration step, 2116 elements

Figure 6: Compression test of biological tissue with two hard lumps: Computed shear modulus distribution for different refinement steps based on the variational error indicator

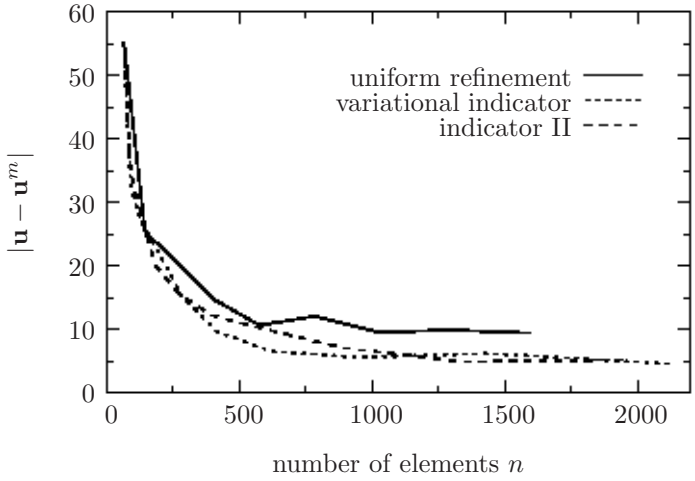

Figure 7: Compression test of biological tissue with two hard lumps: Difference between computed and measured displacement field depending on the number of elements (variational mesh refinement)

This is confirmed by the rate of convergence given in figure 7. Accordingly, the error corresponding the variational mesh adaption decreases much faster than that of the uniform refinement. More precisely, the defined error of an adaptive mesh having only 287 elements is identical to that of a uniform mesh with 1600 elements. Furthermore, the adopted refinement method based on Rivara's LEPP algorithm leads to a nested series of triangulations and hence, a monotonic convergence is guaranteed. For the sake of comparison, the performance of the ad hoc error indicator described in Remark 3.1 is given as well. As evident in figure 7, this indicator leads to a fast convergence as well. However, this cannot be guaranteed in general. Moreover, the variational method is still superior.

5 Clustering technique

Using the aforementioned variational h-refinement, the number of elements and thus, the number of degrees of freedom, increase. In this section, a clustering technique allowing to reduce this number is proposed. It is similar to methods known from digital image compression and leads to an improved efficiency of the advocated finite element method.

5.1 Fundamentals

Consider the benchmark problem shown in figure 2. The optimal discretization would contain only three different shear moduli. Two of them would be associated with the hard lumps, while an additional one would correspond to the surrounding material. Unfortunately, if the solution is not known in advance, the computation of the optimal discretization shows the same complexity as solving the underlying problem. In this section, a clustering technique allowing to reduce the number of degrees of freedom significantly is proposed. It is similar to methods known from digital image compression, where the size of an image file is to be reduced. An important advantage of digital image compression is that the analytical solution, i.e., the original image, is indeed known.

According to [19, 20], two fundamental principles can be applied for compressing a digital image: *loss-free* and *lossy* compression. While in loss-free methods, repeating

Table 1: Algorithm suitable for the elastography inverse problem based on the variational mesh adaption and the clustering technique

1. Initialize: $i = 0$, $\mathcal{T}_0$, n, `TOL`
2. While desired tolerance not attained ($\inf_\mu \mathfrak{g}(\mu) >$ `TOL`), do
   (a) Compute $\mu(\mathbf{X})$ by discrectization $\mathcal{T}_i$ (section 3).
   (b) $i \to i + 1$
   (c) Apply clustering technique (subsection 5.1)
      i. Subdivide $J = [\mu_{\min}, \mu_{\max}]$ equidistantly into n intervals I_j
      ii. Sort shear moduli of elements according to intervals I_j
      iii. Set $\mu_e = \inf(I_j)$ for all elements
   (d) Apply variational mesh adaption (section 4): $\mathcal{T}_{i-1} \to \mathcal{T}_i$
   (e) Apply clustering technique to non-refined elements (compression resulting in n degrees of freedom for non-refined elements)

sequences are detected and stored, lossy strategies are based on a certain rounding procedure. The clustering technique presented here can be considered as a combination of these limiting case. A distinct separation into *loss-free* and *lossy* does not make sense for the inverse problem under investigation, since the underlying shear modulus distribution (the image) is not known.

Conceptually, the shear moduli of the elements are divided grouped. More precisely, before applying variational h-adaption, the maximum and the minimum shear moduli are detected and n intervals all having the same length are generated. Subsequently, the elements are sorted accordingly. Each of these intervals represents one degree of freedom. Hence, the compression ratio is defined by n. The new elements induced by the variational h-adaption are not sorted into these groups. Since the refined elements are usually those at the interfaces and it is not known a priori on which side of the interface the new elements are located, they cannot be sorted at this stage. Clearly, the resulting clustering method is not loss-free, but yields the conservative estimate

$$\inf \mathfrak{g}(\mu^{\text{clust}}) \geq \inf \mathfrak{g}(\mu) \quad \text{since} \quad \mu \in V \supset V^{\text{clust}} \ni \mu^{clust}. \tag{50}$$

The resulting method is summarized in table 1. It is noteworthy that for computations based on measured data showing a certain noise, the clustering technique reduces this artefact.

5.2 Numerical example

The increase in efficiency versus the loss in accuracy of the clustering technique are analyzed in this section by means of the same benchmark as considered already before, see figure 9. The computation starts with the same initial discretization as shown in figure 3(a). Subsequently, the clustering technique with 30 groups is applied. Finally, the variational h-adaption discussed in the previous section is utilized. The resulting discretization serves as a new starting triangulation for the iterative scheme.

Figure 8 shows the shear modulus computed by the variational h-refinement with and without employing the clustering technique. According to this figure, both methods lead

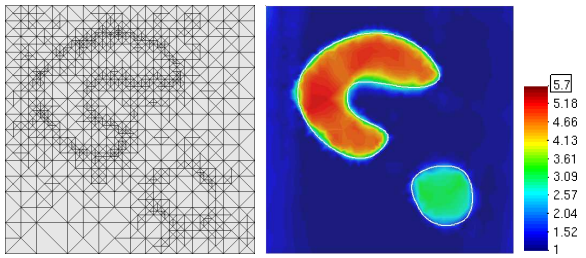

(a) variational h-adaption:
9th iteration step, 2055 elements

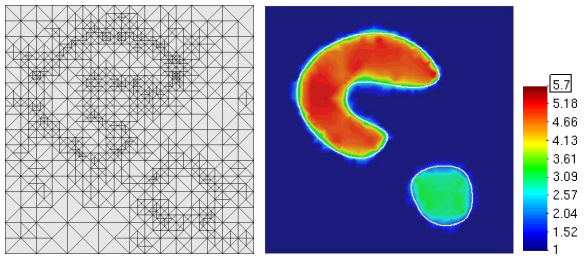

(b) variational h-adaption combined with clustering:
9th iteration step, 1884 elements, 1192 degrees of freedom

Figure 8: Compression test of biological tissue with two hard lumps: Discretization and shear modulus distribution: Variational h-adaption vs. variational h-adaption combined with the clustering technique

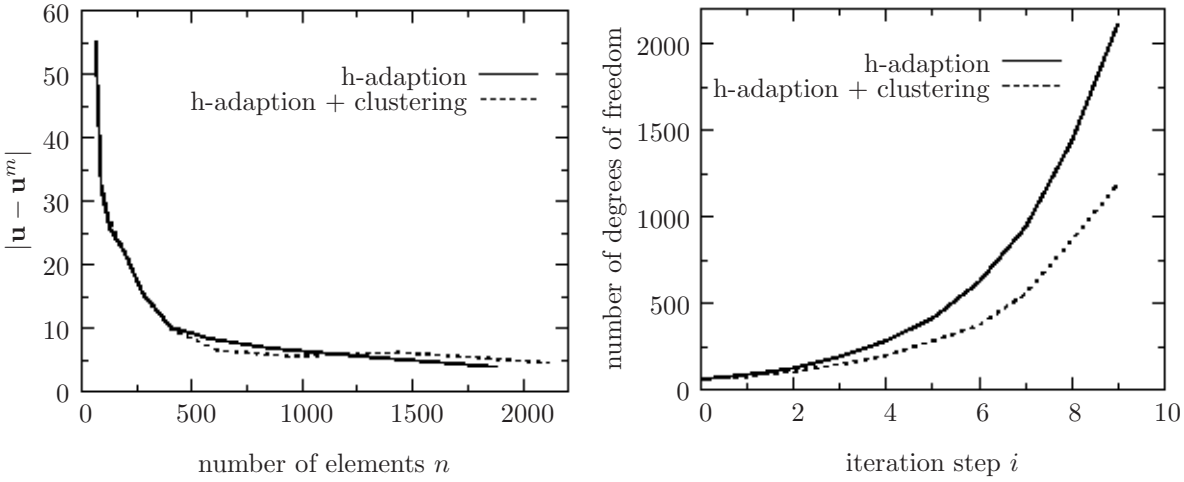

Figure 9: Compression test of biological tissue with two hard lumps: Performance of the variational h-adaption combined with the clustering technique: Left: Rate of convergence; Right: Evolution of the number of degrees of freedom

to almost the same results. The differences are only marginal. A more careful analysis is possible by analyzing figure 9. On the left hand side of figure 9, the rate of convergence is depicted. As evident from this figure, the clustering strategy does not lead to a loss in accuracy. However, it improves the efficiency remarkably. More precisely, the number of degrees of freedom is roughly reduced by a factor of two (right hand side of figure 9). Clearly, by reducing the number of intervals, this ratio can be further increased.

6 Computational efficiency of the novel algorithm

In this section, the efficiency of the novel adaptive scheme, combined with the clustering technique, is critically analyzed. For that purpose, its computing time is compared to that of the standard approach (uniform mesh, no adaptive refinement). The numerical example as considered in the previous sections serves as a benchmark. Since measured data show usually a certain noise, the influence of perturbations with different amplitudes is investigated as well.

For the standard approach, a uniform discretization with 20 x 20 elements is utilized, see figure 3(h), while an initial triangulation consisting of 8 x 8 elements is chosen for

Table 2: Compression test of biological tissue with two hard lumps: Performance and accuracy of the novel adaptive approach compared to the implementation based on a constant uniform mesh

Method	Noise level	Reg. parameter α	$\lvert\mathbf{u}-\mathbf{u}^m\rvert$	$\lvert\mu-\mu^m\rvert/\lvert\mu^m\rvert$	$\Delta t\,[\%]$
Standard	$\Delta = 0.0\%$	0.0	8.38	0.251	-
Adaptive	$\Delta = 0.0\%$	0.0	7.53	0.225	47.7
Standard	$\Delta = 0.5\%$	$7.5 \cdot 10^{-8}$	23.20	0.282	-
Adaptive	$\Delta = 0.5\%$	$7.5 \cdot 10^{-8}$	22.918	0.264	49.7
Standard	$\Delta = 1.0\%$	$2.5 \cdot 10^{-7}$	40.725	0.305	-
Adaptive	$\Delta = 1.0\%$	$2.5 \cdot 10^{-7}$	40.642	0.294	27.4
Standard	$\Delta = 2.0\%$	$7.5 \cdot 10^{-7}$	77.565	0.344	-
Adaptive	$\Delta = 2.0\%$	$7.5 \cdot 10^{-7}$	77.414	0.326	18.0

the novel adaptive implementation, see figure 3(b). Within all computations, the initial shear modulus is set to $\mu = 1$. Based on the initial mesh (8 x 8), the variational adaptive scheme, combined with the clustering technique (30 intervals), is applied. Independent of the added noise level, four refinement and clustering steps led to a solution showing a better accuracy than that of the standard approach (uniform 20 x 20 mesh).

The results are summarized in figure 10 and table 2. According to figure 10, the standard approach based on a uniform mesh underestimates the shear modulus, if the noise level is increased. A similar tendency is also observed for the novel adaptive method. However, it is significantly less pronounced. Furthermore, it is evident that although the adaptive scheme automatically detects the interfaces between domains showing different shear moduli, it refines other domains as well, if the noise amplitude reaches a certain threshold. Clearly, this is not surprising, since the algorithm in its present form does not distinguish between real tumors (the physical shear modulus is comparatively large) and artificial tumors (the measured shear modulus is comparatively large). However, additional criteria for detecting only the real tumors can easily be integrated within the advocated method. For instance, the diameter of real tumors is usually larger than that of its artificial counterparts being defined by the resolution of the measuring device. Hence, only regions larger than that threshold are associated with real tumors and thus, the mesh has to be refined only within such regions.

A quantitative comparison between the novel adaptive approach (denoted as *Adaptive* within table 2) and that based on a constant uniform mesh (denoted as *Standard* within table 2) is given in table 2. Accordingly, three non-vanishing noise levels $\Delta = 0.5\%$, $\Delta = 1.0\%$ and $\Delta = 2.0\%$ with the respective regularization parameters $\alpha = 7.5 \cdot 10^{-8}$, $\alpha = 2.5 \cdot 10^{-7}$ and $\alpha = 7.5 \cdot 10^{-7}$ are considered. The accuracy of both methods is checked by monitoring the displacement error ($|\mathbf{u}-\mathbf{u}^m|$) as well as the relative error in the shear modulus ($|\mu-\mu^m|/|\mu^m|$). As evident from table 2, the novel adaptive scheme was stopped, when its accuracy was better than that of the standard approach. For that purpose, four adaptive and four clustering steps were required, independent of the noise level.

Clearly, the proposed variational mesh adaption guarantees an improvement of the solution. Therefore, by applying this method successively, it was expected that it led finally to a better accuracy than that of the standard approach. However, it is very difficult to estimate the numerical efficiency of this novel method. For that purpose, the computing times were critically analyzed. The results are shown in table 2. Here,

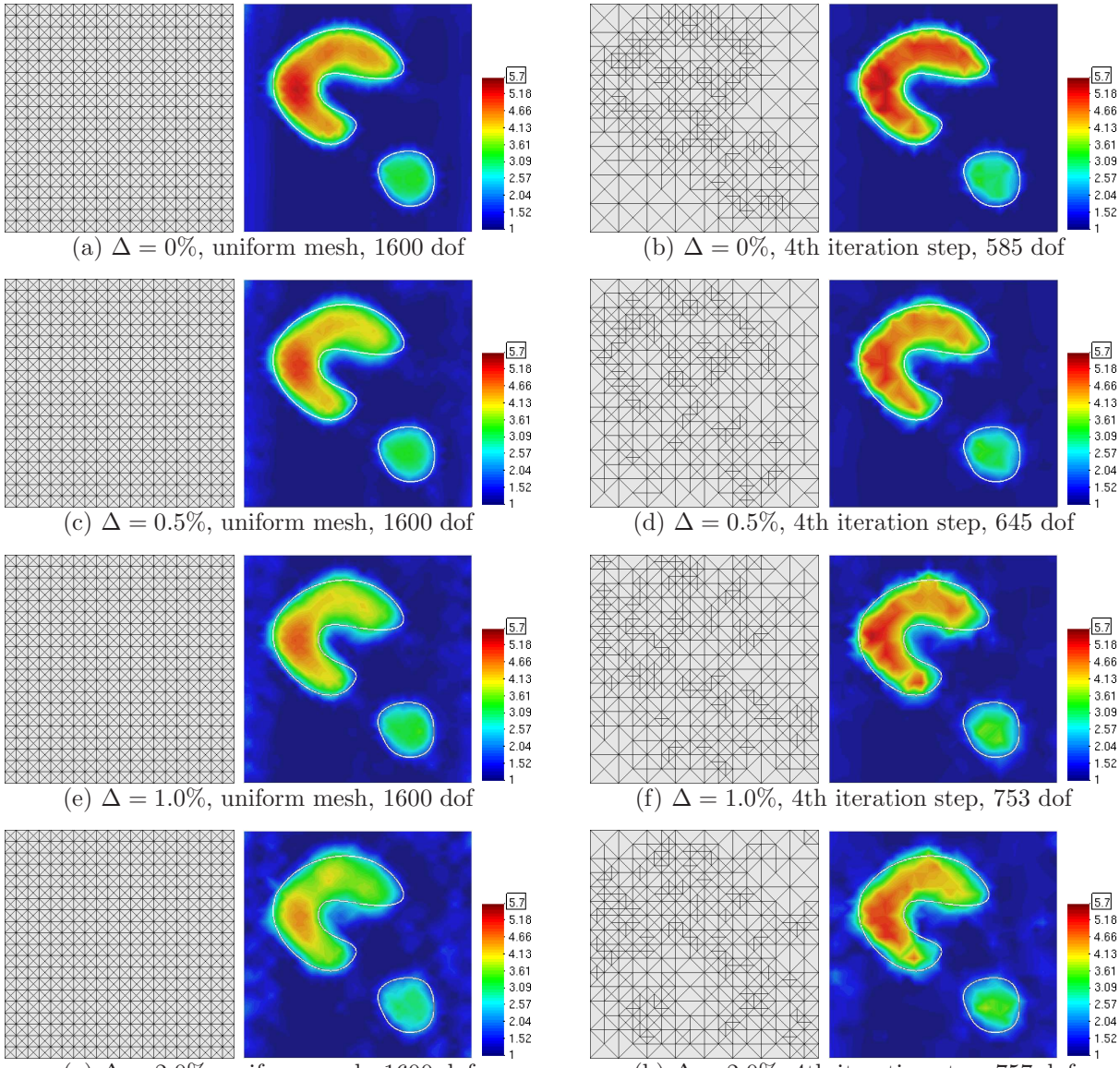

(a) $\Delta = 0\%$, uniform mesh, 1600 dof (b) $\Delta = 0\%$, 4th iteration step, 585 dof

(c) $\Delta = 0.5\%$, uniform mesh, 1600 dof (d) $\Delta = 0.5\%$, 4th iteration step, 645 dof

(e) $\Delta = 1.0\%$, uniform mesh, 1600 dof (f) $\Delta = 1.0\%$, 4th iteration step, 753 dof

(g) $\Delta = 2.0\%$, uniform mesh, 1600 dof (h) $\Delta = 2.0\%$, 4th iteration step, 757 dof

Figure 10: Compression test of biological tissue with two hard lumps: Discretizations and computed shear modulus distribution; left hand side: standard approach based on a uniform and constant mesh; right hand side: novel adaptive method combined with the clustering technique. The noise-level is denoted as Δ.

Δt denotes the relative reduction in computing time. According to table 2, the adaptive method allows to reduce the overall time by a factor of 2, if the noise level is comparatively low. However, even in case of considerably high noise, the algorithm is very efficient (18% reduction in computing time).

It is noteworthy that in contrast to the standard approach based on a constant uniform mesh, the implementation of the adaptive method has not been optimized, i.e., the reported data are conservative. For instance, the computation of the error indicator which is relatively time consuming can be easily implemented in parallel. By doing so, a significant boost in efficiency can be easily obtained.

7 Conclusions

In this paper, a novel numerical implementation suitable for the elastography inverse problem has been proposed. Focus was on the efficiency of the algorithmic formulation. This is of particular interest for a successful application of this method for detecting tumors in medical practice. For improving the efficiency of the numerical implementation, two different methods have been proposed and finally, coupled to one another: a variational mesh adaption and a clustering technique. Naturally relying on the underlying minimization principle governing the inverse problem, the finite element discretization is only refined locally within the variational approach, if this has a significant effect on the function to be minimized, i.e., if the error is reduced considerably. The proposed error indicator shows linear complexity and hence, it is very efficient. The performance of the algorithm was further improved by elaborating a clustering technique allowing to reduce the number of unknowns explicitly. A positive side effect of this method is that data noise is naturally reduced (smoothing of the solution). Numerical analyses of a realistic benchmark problem clearly demonstrated the performance of the resulting finite element method.

References

[1] J. Ophir, I. Céspedes, H. Ponnekanti, Y. Yazdi, and X. Li. Elastography: A quantitive method for imaging the elasticity of biological tissues. *Ultrasonic Imaging*, 13:111–34, 1991.

[2] B. S. Garra, E. I. Cespedes, J. Ophir, S. R. Spratt, R. A. Zuurbier, C. M Magnant, and M. F. Pennanen. Elastography of breast lesions: initial clinical results. *Radiology*, 202:79–86, 1997.

[3] F. Kallel and M. Bertrand. Tissue elasticity reconstruction using linear perturbation method. *IEEE Transactions on Medical Imaging*, 15(3):299–313, 1996.

[4] M. M. Doyley, P. M. Meaney, and J. C. Bamber. Evaluation of an iterative reconstruction method for quantitative elastography. *Physics in Medicine and Biology*, 45(6):1521–40, 2000.

[5] A. A. Oberai, N. H. Gokhale, and G. R. Feijo. Solution of inverse problems in elasticity imaging using the adjoint method. *Inverse Problems*, 19(2):297–313, 2003.

[6] W. A. M. Khaled. *Displacement estimation analyses for reconstructive ultrasound elastography using finite-amplitude deformations*. PhD thesis, Ruhr-Universität Bochum, 2007.

[7] S. Reichling. *Das inverse Problem der quantitativen Ultraschallelastografie unter Berücksichtigung großer Deformationen*. PhD thesis, Ruhr-Universität Bochum, 2007.

[8] M. O'Donnell, A. R. Skovoroda, B. M. Shapo, and S.Y. Emelianov. Internal displacement and strain imaging using ultrasonic speckletracking. *IEEE transactions on ultrasonics, ferroelectrics, and frequency control*, 41:314–25, 1994.

[9] C. Pellot-Barakat, F. Frouin, M.F. Insana, and A. Herment. Ultrasound elastography based on multiscale estimations of regularized displacement fields. *IEEE Transactions on Medical Imaging*, 23:153–63, 2004.

[10] C. Sumi, A. Suzuki, and K. Nakayama. Estimation of shear modulus distribution in soft tissue from strain distribution. *IEEE Transactions on Biomedical Engineering*, 42(2):193–202, 1995.

[11] A. R. Skovoroda, S. Y. Emelianov, and M. O'Donnell. Tissue elasticity reconstruction based on ultrasonic displacement and strain images. *IEEE Transactions on Ultrasonics, Ferroelectrics and Frequency Control*, 42(4):747–65, 1995.

[12] A. A. Oberai, N. H. Gokhale, M. M. Doyley, and J. C. Bamber. Evaluation of the adjoint equation based algorithm for elasticity imaging. *Physics in Medicine and Biology*, 49:2955–74, 2004.

[13] N. H. Gokhale, P. E. Barbone, and A. A. Oberai. Solution of the nonlinear elasticity imaging inverse problem: the compressible case. *Inverse Problems*, 24:26pp, 2008.

[14] R. Verfürth. *A Review of A Posteriori Error Estimation and Adaptive Mesh-Refinement Techniques*. Wiley-Teubner, 1996.

[15] M. Ainsworth and J. T. Oden. *A Posteriori Error Estimation in Finite Element Analysis*. Wiley, 2000.

[16] P.G. Ciarlet. *Mathematical elasticity, volume I: Three-dimensional elasticity*. Springer Netherlands, 1988.

[17] J. Mosler and M. Ortiz. Variational h-adaption in finite deformation elasticity and plasticity. *International Journal for Numerical Methods in Engineering*, 72:505–23, 2007.

[18] B. Dacorogna. *Direct Methods in the Calculus of Variations*. New York: Springer, 1989.

[19] D. Salomon. *Data Compression: The Complete Reference*. Springer Verlag, 2000.

[20] W. G. Kropatsch and H. Bishof. *Digital Image Analysis*. Springer-Verlag New York, 2001.

[21] C. Truesdell and W. Noll. *The Non-Linear Field Theories of Mechanics*. Springer-Verlag, 3rd edition, 2004.

[22] J. E. Marsden and T. J. R. Hughes. *Mathematical Foundations of Elasticity*. Dover Publications, 1994.

[23] K. Washizu. *Variational Methods in Elasticity and Plasticity*. Pergamon Press, 3 edition, 1982.

[24] Y. C. Fung. *Biomechanics: Mechanical Properties of Living Tissues*. Springer, 1993.

[25] P. Wriggers. *Nonlinear Finite Element Methods*. Springer, 2009.

[26] J. C. Simo and T. J. R. Hughes. *Computational Inelasticity*, volume 7 of *Interdisciplinary Applied Mathematics*. Springer-Verlag, New York, 1998.

[27] O. C. Zienkiewicz and R. L. Taylor. *The Finite Element Method*, volume 1. Butterworth-Heinemann, 5 edition, 2000.

[28] J. C. Simo, R. L. Taylor, and K. S. Pister. Variational and projection methods for the volume constraint in finite deformation elasto-plasticity. *Computer Methods in Applied Mechanics and Engineering*, 51:177–208, 1985.

[29] J. C. Simo and R. L. Taylor. Quasi-incompressible finite elasticity in principal stretches. continuum basis and numerical algorithms. *Computer Methods in Applied Mechanics and Engineering*, 85:273–310, 1991.

[30] T. J. R. Hughes. *The Finite Element Method*. Dover Publications, 2000.

[31] O. Schenk and K. Gärtner. Solving unsymmetric sparse systems of linear equations with pardiso. *Journal of Future Generation Computer Systems*, 20:475–87, 2004.

[32] O. Schenk and K. Gärtner. On fast factorization pivoting methods for sparse symmetric indefinite systems. *Electronic Transactions on Numerical Analysis*, 23:158–79, 2006.

[33] H. Engl, M. Hanke, and A. Neubauer. *Regularization of Inverse Problems*. Kluwer Academic Publishers, 2003.

[34] Richard H. Byrd, Peihuang Lu, Jorge Nocedal, and Ciyou Zhu. A limited memory algorithm for bound constrained optimization. *SIAM Journal on Scientific Computing*, 16:1190–208, 1994.

[35] C. Zhu, R. H. Byrd, P. Lu, and J. Nocedal. Algorithm 778: L-bfgs-b: Fortran subroutines for large-scale bound-constrained optimization. *ACM Transactions on Mathematical Software*, 23:550–60, 1997.

[36] M.-C. Rivara. Local modification of meshes for adaptive and/or multigrid finite-element methods. *Journal of Computational and Applied Mathematics*, 36:79–89, 1991.

[37] M.-C. Rivara. New mathematical tools and techniques for the refinement and/or improvement of unstructured triangulations. *International Journal for Numerical Methods in Engineering*, 40:3313–24, 1997.

[38] P. Thoutireddy and M. Ortiz. A variational r-adaption and shape-optimization method for finite-deformation elasticity. *International Journal for Numerical Methods in Engineering*, 61:1–21, 2004.

[39] G.M. McNeice and P.V. Marcal. Optimization of finite-element grids based on minumum potential-energy. *Journal of Engineering for Industry-Transactions of the ASME*, 95(1):186–90, 1973.

[40] C. Felippa. Numerical experiments in finite element grid optimization by direct energy search. *Appl. Math. Modelling*, 1:93–6, 1976.

[41] M. Braun. Configurational forces induced by finite element discretization,. *Proc. Estonian Acad. Sci. Phys. Math.*, 46:24–31, 1997.

[42] E. Kuhl, H. Askes, and P. Steinmann. An ALE formulation based on spatial and material settings of continuum mechanics. Part 1: Generic hyperelastic formulation. *Computer Methods in Applied Mechanics and Engineering*, 193(39-41):4207–22, 2004.

[43] J. Mosler and M. Ortiz. On the numerical modeling of variational arbitrary lagrangian-eulerian (vale) formulations. *International Journal for Numerical Methods in Engineering*, 67:1272–89, 2006.

[44] J. Mosler. *On the numerical modeling of localized material failure at finite strains by means of variational mesh adaption and cohesive elements.* Habilitation, Ruhr University Bochum, Germany, 2007.

[45] P. V. McNeice, G. M. ; Marcal. Optimization of finite element grids based on minimum potential energy. *Trans. ASME, J. of Eng. for Industry*, 95:186–90, 1973.

[46] C. A. Felippa. Numerical experiments in finite element grid optimization by direct energy search. *Applied Mathematical Modelling*, 1:239–44, 1976.